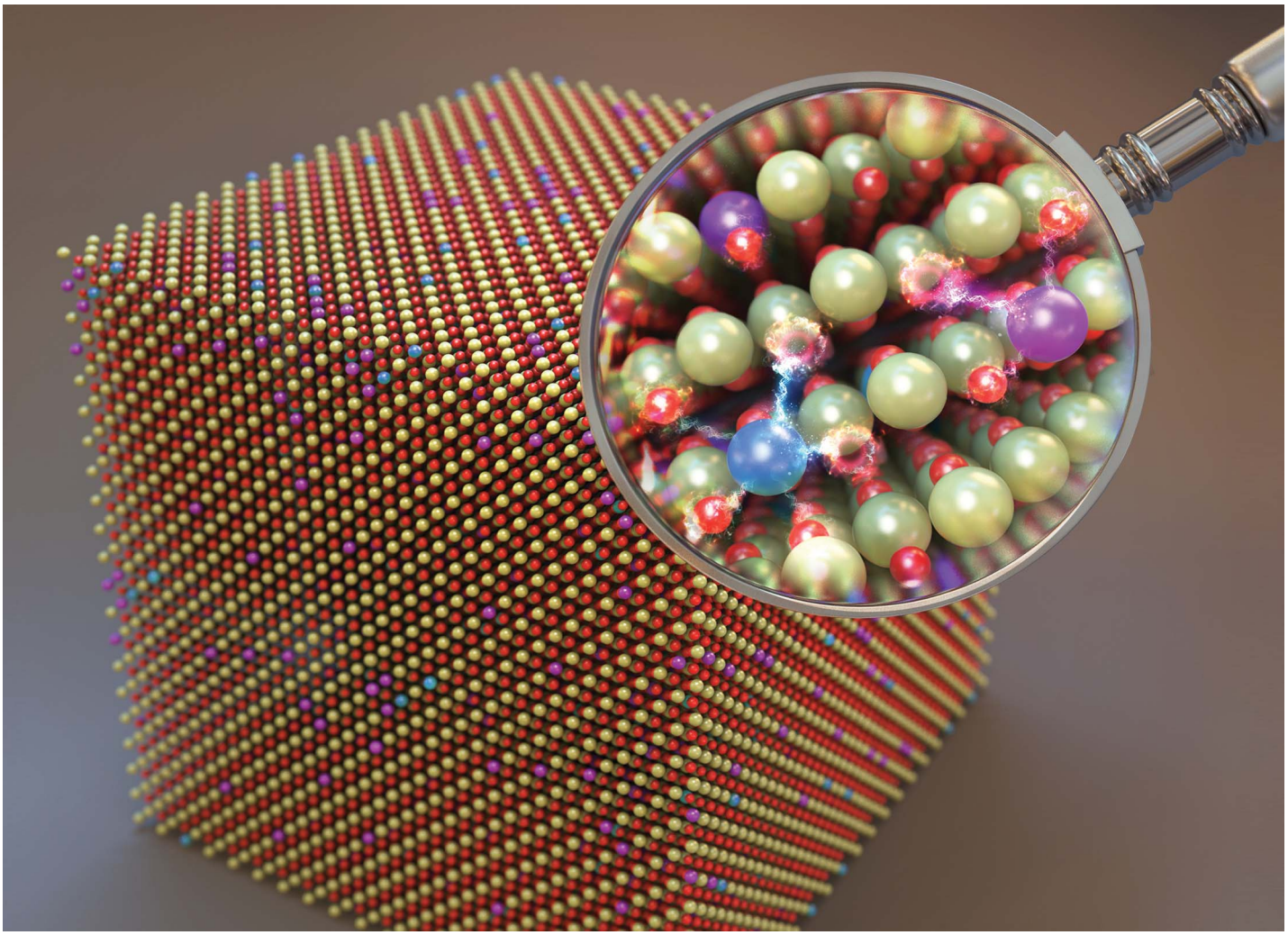

Highlighting research from a team led by Dr Kwang-Ryeol Lee at Korea Institute of Science and Technology.

Oxygen ion transport in doped ceria: effect of vacancy trapping

This work theoretically revealed that the oxygen vacancy trapping by dopants governs the oxygen conductance in the ceria-based electrolyte of solid oxide fuel cell. Multiscale simulation of Gd doped ceria with La or Y co-dopants shows an intimate relationship between the oxygen diffusion and the oxygen vacancy trapping, regardless of the energy barrier against the oxygen migration in the co-doped ceria.

As featured in:

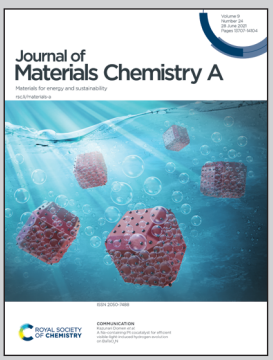

See Kwang-Ryeol Lee *et al.*, *J. Mater. Chem. A*, 2021, **9**, 13883.

ROYAL SOCIETY OF CHEMISTRY

rsc.li/materials-a

Registered charity number: 207890

Journal of Materials Chemistry A

ROYAL SOCIETY OF CHEMISTRY

PAPER

Cite this: *J. Mater. Chem. A*, 2021, **9**, 13883

Oxygen ion transport in doped ceria: effect of vacancy trapping†

Mehmet Emin Kilic, [a] Jong-Ho Lee [b] and Kwang-Ryeol Lee*[a]

Received 1st February 2021
Accepted 5th May 2021

DOI: 10.1039/d1ta00926e

rsc.li/materials-a

Trivalent dopants in the CeO_2 lattice generate oxygen vacancies in the lattice, which is vital to oxygen diffusion. However, the dopants also have two detrimental effects on the oxygen vacancy migration: trapping the oxygen vacancies in the dopant and blocking the vacancy migration by increasing the energy barrier for the vacancy transport. We studied the diffusion of oxygen in Gd doped CeO_2 with La or Y co-dopants by using molecular dynamics (MD) simulation and compared them with the vacancy trapping and blocking behavior by the dopants. The trapping was characterized by the coordination number (CN) of cations statistically analyzed on a large scale. The blocking caused by the dopants was investigated by first principles nudged elastic band analysis. We found that the oxygen diffusion measured by the mean square displacement of oxygen in doped CeO_2 is enhanced when the trapping of oxygen vacancies is reduced by the co-doping. In contrast, the change in the energy barrier against oxygen migration in the co-doped lattice is not consistent with the diffusion behavior. This result evidently shows that the oxygen ion transport is governed by the trapping of oxygen vacancies.

1 Introduction

The ionic conductivity of CeO_2 based materials has been extensively studied for their application in high performance electrolytes for solid oxide fuel cells (SOFCs).[1–3] The doping of trivalent ions such as Sm, Sc, Gd, Y, or La has been widely employed to increase the ionic conductivity (typically, 2–3 orders of magnitude higher than that of yttria-stabilized zirconia below 600 °C).[4] Scientific understanding of the oxygen transport mechanism would be crucial for structure optimization of electrolyte materials of SOFCs or further design of novel electrolytes. Since the substitutional doping with trivalent species generates oxygen vacancies that facilitate oxygen ion transport, the distribution and mobility of the vacancies in the doped ceria is crucial to understand the ion transport behavior. Doping or external strain is broadly considered to improve the ion transport in thin film SOFCs.[5–8] However, the mechanism governing the ion transport was not evident and various mechanisms like vacancy trapping, vacancy migration blocking, configuration entropy or lattice strain due to the difference in the ionic radius of dopants were suggested to explain the experimental observations.[8–12]

In doped ceria, the ionic conductivity steadily increases with increasing dopant concentration up to a maximum at about 8–20 mol% depending on the type of dopant.[13,14] Above the optimum concentration, a significant increase in the vacancy-dopant interaction causes a sharp reduction of the ionic conductivity.[15] It was also reported that there exists an optimum size of the dopant for improved ionic conductivity, which would be correlated with the dopant oxygen vacancy interactions. Butler *et al.* showed that the vacancy-dopant interaction is largely dependent on the ionic radius of dopants.[16] Minervini *et al.* reported that the minimum interaction was observed when the size of the dopant is close to that of the host cation, Ce.[17] Gd was considered as an optimized dopant, since the size of Gd^{3+} is close to that of the host cation.[18–20] However, the ion conductivity was not simply correlated with the ion size of dopants because the dopant–vacancy interactions result in both vacancy trapping and the blocking of vacancy migration. It was reported that the optimum dopant size was obtained when these two effects are balanced.[21]

External strain also affects the conductivity of doped ceria electrolyte materials: the conductivity was improved under tensile strain. The external strain effect has drawn much attention as an additional method to manipulate the ion conductivity. This phenomenon is qualitatively discussed in terms of the complicated interactions between defects, where activation energy is a sum of migration enthalpy and associate formation enthalpy between the defects.[8] Applied tensile strain would reduce the migration enthalpy by expanding the cation

[a]*Computational Science Center, Korea Institute of Science and Technology, Seoul, Republic of Korea. E-mail: krlee@kist.re.kr*

[b]*Center for Energy Materials Research, Korea Institute of Science and Technology, Seoul, Republic of Korea*

† Electronic supplementary information (ESI) available: Structure relaxation; computational details; lattice constants of CeO_2 and GDC; radial distribution functions; energy *vs.* volume curves; mean square displacement of GDC, LDC, and YDC; variation of stress with respect to applied tensile strains. See DOI: 10.1039/d1ta00926e

lattice network through which the oxygen ion migrates to the next vacancy site. Rushton *et al.* reported that the tensile strain decreases the preferential association of vacancies with dopants, whereas the compressive strain increases the association.[22] The enhanced diffusion of oxygen under tensile strain was explained by the reduced binding energy between the vacancy and the dopant.[23] On the other hand, Ahn *et al.* theoretically investigated the strain effect on the migration barrier in Gd doped CeO_2 thin films.[24] They reported that the barrier energy corresponds to the tetrahedron volume, which can be manipulated by the dopant configuration and the number of dopants. Many MD simulations showed the consistent result of the strain effect.[22,23,25,26] However, theoretical analysis beyond the phenomenological description of the diffusion behavior is yet to be reported.

The vacancy-dopant interaction was extensively discussed in terms of the trapping and the blocking due to the dopants.[21] The strong interaction between the vacancy and dopant cations may trap the oxygen vacancies into the dopant, forming a vacancy-dopant cluster.[16] In addition, dopants of different sizes can induce lattice distortion that modifies the energy barrier against the oxygen ion transport.[27] Both trapping and blocking of oxygen vacancies by dopants may result from the coulombic interaction due to the effective charge of two defects and elastic strain field caused by the size mismatch between the host and the dopant cations.[28,29] Therefore, these two effects are hardly separated to reveal the dominating mechanism to control the ion transport.

In the present work, theoretical investigations of a co-doped ceria system enabled us to reveal that the trapping of oxygen vacancies dominates the ion transport. It can be suggested that the engineering of vacancy trapping is the most effective to optimize the ion transport in ceria electrolytes. We studied the oxygen diffusion in a multi-doped ceria electrolyte by employing both statistical molecular dynamics simulation and first principles microscopic calculations. Statistical analysis of the diffusion and the coordination number of cations on a large scale shows an intimate relationship between the ion transport and the vacancy trapping behavior in single- and co-doped ceria. In contrast, the energy barrier of oxygen vacancy migration was inconsistent with the simulated oxygen diffusion behavior under various doping conditions.

2 Computational methods

2.1 Density of functional calculations

First-principles calculations based on density functional theory (DFT) are performed using the Vienna *Ab initio* Simulation Package (VASP).[30,31] The projector augmented wave (PAW) method is employed.[32] The electron exchange and correlation potentials are treated in the generalized gradient approximation (GGA) using the parameterization of Perdew, Burke and Ernzerhof.[33] The DFT + U_{eff} method is applied to the 4f electrons of ceria, introduced by Dudarev *et al.*,[34] where an effective Hubbard term ($U_{\text{eff}} = U - J$) is described by the difference between the on-site Coulomb (U) and on-site exchange (J) terms. In the current investigation, the U_{eff} value is only considered for the Ce 4f states. A kinetic energy cut-off of 500 eV is used for all DFT calculations to expand the wave functions in the plane-basis set. The Brillouin-zone (BZ) integrations are performed using a Monkhorst–Pack scheme.[35] We utilized a 24 × 24 × 24 k-point mesh for the 1 × 1 × 1 CeO_2 conventional unit cell, which is accurate enough based on our test calculations. The convergence criteria for the total energies and forces are set within 10^{-5} eV and 0.01 eV Å^{-1}, respectively. To examine the oxygen migration barrier in doped ceria, the climbing-image NEB[36] method was used to find minimum energy paths (MEPs) and transition states (TSs) from given the initial state (IS) and final state (FS). The IS and FS have taken the same cell shape and volume. An interpolated chain of configurations (images) between IS and FS positions were connected by springs and relaxed simultaneously. Five linearly interpolated images between the IS and FS for single oxygen ion diffusion were taken. All the images were relaxed until the maximum force acting on atom was less than 0.01 eV Å^{-1}. The saddle point was then verified to be the true TS.

2.2 Molecular dynamics and lattice dynamics calculations

The classical MD and lattice dynamics (LD) simulations are performed using the LAMMPS[39] and the GULP code,[40] respectively. The effective potential of inter-atomic interactions between i and j ions is considered as a Buckingham-type potential with a long-range coulombic term:

$$V(r_{ij}) = \frac{q_i q_i}{r_{ij}} + A_{ij}\exp\left(\frac{r_{ij}}{\rho_{ij}}\right) - \frac{C_{ij}}{r_{ij}^{6}} \quad (1)$$

where q_i represents the charge of ion i, r_{ij} is the inter-ionic distance, and other A_{ij}, ρ_{ij}, and C_{ij} parameters are used to represent the short-range terms for each element. A cut-off range of 12 Å was applied for the short-range terms. The potential parameters for Ce^{4+}–O^{2-}, Gd^{3+}–O^{2-}, Y^{3+}–O^{2-}, La^{3+}–O^{2-}, and O^{2-}–O^{2-}, given in Table 1, have already been successfully employed to describe the dynamic properties of doped ceria.[23,41] In the case of cation–cation interactions, the forces are assumed to be purely coulombic since cations are generally smaller than the oxygen ion.[17,37,38,42] The Coulomb interactions are summed up using Ewald's method with the formal charges of the ions.[43] The analysis of the electronic structure of ceria shows that it is largely ionic in nature.[44] The time step used for the integration of Newton's equations of motion is set to 0.5 fs. The temperature T and the pressure P are controlled *via* a Nosé–Hoover thermostat and barostat, respectively.[45–47] The Buckingham-type potential model has already

Table 1 Inter-ionic potential parameters employed in the MD and LD simulations

i–j	A_{ij} (eV)	ρ (Å)	C_{ij} (eV Å^6)	Ref.
Ce^{4+}–O^{2-}	1809.68	0.3547	20.40	37
Gd^{3+}–O^{2-}	1885.75	0.3399	20.34	17
Y^{3+}–O^{2-}	1766.40	0.33849	19.43	38
La^{3+}–O^{2-}	2088.79	0.3460	23.25	17
O^{2-}–O^{2-}	9547.96	0.2192	32.0	38

been successfully employed to describe the dynamic properties of ceria-based materials in previous literature.[48–50] The details of the structural relaxation process and computational details are explained in the ESI.†

3 Results and discussion

The oxygen vacancies in the electrolyte of SOFCs play a crucial role in anion transport. Their interaction with cations or other oxygen vacancies would radically affect the ionic conductivity. We first examined the equilibrium configuration of oxygen ion vacancies in 12.5 mol% Gd doped ceria systems by energetics calculation at 0 K. Fig. 1 shows the procedure to find the equilibrium configuration. For a ceria solid solution that contains 12.5 mol% Gd, we replaced 4 Ce^{4+} ions in the 2 × 2 × 2 CeO_2 supercell with Gd^{3+} ions. Two oxygen vacancies were then introduced to maintain the electrical neutrality of the system. There are about 43 million possible configurations. Considering the equivalent lattice sites, we selected 145 152 irreducible configurations using the Site-Occupation Disorder (SOD) algorithm.[51] The irreducible configuration is composed of 72 distinguishable Gd ion configurations with 2016 oxygen vacancy configurations for each Gd ion configuration. To have a statistical glimpse of the energetics of the 145 152 configurations, we first used empirical-potential lattice dynamics (LD) calculations to find the minimum energy configuration of vacancies for a given Gd configuration. From the LD calculation results, we chose 72 lowest energy configurations for each Gd configuration. The energies of the 72 configurations were marked in blue in Fig. 1(a). More accurate values of the energy

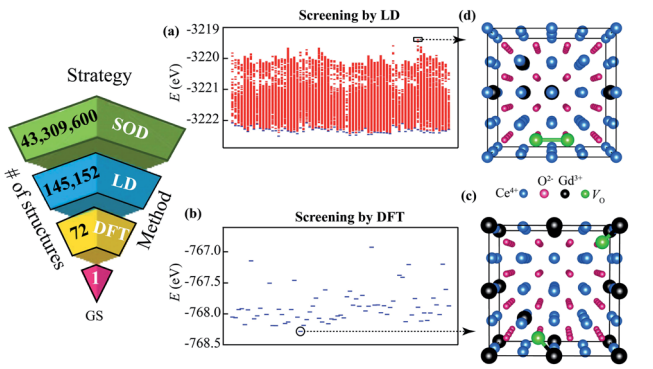

Fig. 1 Energetic screening of 12.5 mol% GDC, where 4 Gd^{3+} substituted with 4 Ce^{4+} and generated 2 oxygen vacancies (V_O) in the c-$C_{32}O_{64}$ system. For this stoichiometry, there are 43 309 600 configurations, which reduced to 145 152 configurations by excluding the equivalent sites using the SOD. (a) The total energy distribution of the 145 152 configurations calculated by using LD simulations. Here, there are 72 columns. Each column, containing 2016 configurations, corresponds to the same substituted position of gadolinium ions, and the data in the same columns correspond to the different positions of oxygen vacancies. (b) Total energy of the lowest energy configurations of the 72 columns (marked in blue in (a)), obtained by the DFT calculation. (c) The most favorable atomic configuration of the lowest total energy among all the configurations (marked by the circle in (b)). (d) An example of the unfavorable atomic configurations of the highest energy (marked by the square in (a)).

were calculated in the DFT framework as shown in Fig. 1(b). We found the most favorable configuration as shown in Fig. 1(c), the energy of which was marked by the circle in Fig. 1(b). It is evident that the oxygen vacancies tend to exist near doped Gd^{3+} (black sphere) rather than Ce^{4+} (blue sphere). The preferred interaction would be due to the smaller charge of Gd^{3+} than that of Ce^{4+}, where the effective charge of Gd^{3+} is −1 yielding an attractive force on the oxygen vacancy with an effective charge of +2. On the other hand, divacancy formation is the most unfavorable in the Gd doped ceria system. High energy configurations marked by the square in Fig. 1(a) is associated with the divacancy formation as shown in Fig. 1(d).

The coordination number (CN) of the doped and host cations was analyzed *via* molecular dynamics simulation to illustrate the interaction behavior of oxygen vacancies on a much larger scale. For the MD simulation, we employed the same inter-ionic potential parameters as in the LD calculation (Table 1) and constructed a doped ceria model using CeO_2 crystals of total 12 000 ions (4000 Ce^{4+} and 8000 O^{2-}). 10 mol% Gd doped CeO_2, referred to as 10GDC, was modeled by randomly substituting 400 Ce^{4+} with Gd^{3+} and removing 200 O^{2-} to maintain electrical charge neutrality. For the co-doped CeO_2 system, we studied two different models: yttrium (Y^{3+}) or lanthanum (La^{3+}) co-doped GDC, where 3 mol% Gd^{3+} is replaced by Y^{3+} (referred to as 3Y7GDC) or La^{3+} (referred to as 3La7GDC). The role of the ionic radius could be systematically studied in the present work, since La^{3+} (130.0 pm) is larger than Gd^{3+} (119.3 pm), while Y^{3+} (115.9 pm) is smaller.[52] These models were annealed at 2000 K to relax the artificial atomic structure before analyzing the CN of cations at 1273 K, which is the typical operating temperature of SOFCs. The details of the relaxation process are reported in the ESI.† The CN of a cation was estimated from the number of ions within the cut-off radius (0.35 nm) of the cation. The cut-off radius was chosen according to the first minima after the first nearest peak of the radial distribution function at 1273 K (see Fig. S1†). The radial distribution function also showed that the crystallinity of the co-doped ceria is well maintained at 1273 K. The CN of the cations was monitored for 1 ns. For better statistics, five different configurations of a given doped composition were used to analyze the CN.

Fig. 2 shows the CN of cations with oxygen ions at 1273 K for 1 ns. The CN of cations is found to be lower than that of perfect fluorite oxide, 8, because of the anion vacancies around them. It must be noted in Fig. 2(a) that the CN of Gd^{3+} is obviously lower than that of Ce^{4+} in 10GDC. This result indicates that the average number of oxygen vacancies bound to Gd^{3+} is larger than that to Ce^{4+}, consistent with the equilibrium configuration of GDC depicted in Fig. 1(c). The preferred interaction between the oxygen vacancy and the Gd dopant may have a deleterious effect on the oxygen diffusion since the anion migration needs to overcome the trapping of the oxygen vacancy in the Gd ion. It was found that the co-doping of GDC with Y^{3+} or La^{3+} significantly changes the preferred interaction of the vacancy with the cations. Fig. 2(b) and (c) show the CN data for 3Y7GDC and 3La7GDC, respectively. When Y^{3+} is co-doped, the CN of Y^{3+} appears to be smaller than that of Gd^{3+}, while the CN of Ce^{4+}

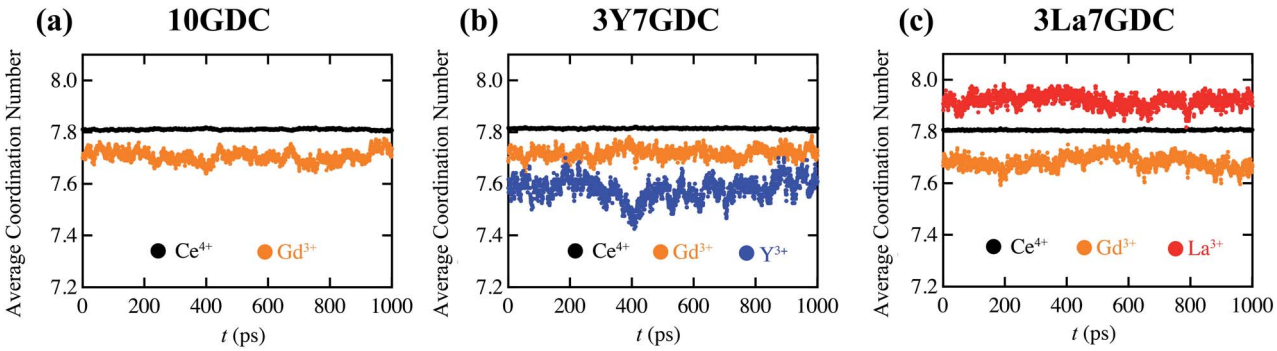

Fig. 2 The coordination number (CN) of cations (Ce^{4+}, Gd^{3+}, Y^{3+}, and La^{3+} ions) at $T = 1273$ K as a function of time for 1 ns (a) in 10GDC, (b) in 3Y7GDC, and (c) in 3La7GDC. The CN of Ce^{4+} in ideal cubic ceria is 8.

increases to slightly larger than 7.8 (see Fig. 2(b)). This result shows the strong preference of the oxygen vacancy to Y^{3+} compared to both Ce^{4+} and Gd^{3+}. In contrast, Fig. 2(c) shows that the CN of La^{3+} is even higher than that of Ce^{4+} with a slight decrease in the CN of Gd^{3+}. The higher CN of La^{3+} ions indicates the less preference of oxygen vacancies to the La^{3+} dopant, while the CN of Gd^{3+} slightly decreased. This behavior is consistent with the previous nuclear magnetic resonance analysis of La doped ceria.[53]

The change of the preference would be understood in terms of the ionic radii of Gd^{3+}, Y^{3+}, and La^{3+}.[52] We noticed an increase in the equilibrium lattice volume by oxygen vacancy incorporation (Fig. S2†), which reveals that the effective size of oxygen vacancies is larger than that of oxygen anions. Because the ionic radius of Y^{3+} is smaller than that of Gd^{3+}, Y co-doping can induce a larger free space that can attract the oxygen vacancy. Opposite behavior would occur in the case of La^{3+} co-doping, since the ionic radius of La^{3+} is much larger than that of Gd^{3+}. In the recent study of defect association energy by Koettgen *et al.*,[21] the oxygen vacancy prefers the second nearest neighbor site of the La^{3+} dopant, although the vacancy is strongly trapped by the Y^{3+} dopant.

Fig. 3(a) shows the mean square displacement (MSD) of ions of 10GDC in major crystalline directions, <001>. In order to enhance the jumping event of oxygen vacancies, the diffusion simulation was performed at higher temperature (1800 K) than the typical operating temperature (1273 K). The MSD, $\langle \Delta R^2 \rangle$ data were obtained from the MD simulations for 1 ns using eqn (1).

$$\langle \Delta R^2 \rangle = \frac{1}{N}\sum_{i=1}^{N}\{R_i(t+\Delta t) - R_i(t)\}^2 \quad (2)$$

where $R(t)$ is the position of ions at time t, Δt is the time step and N is the total number of ions. The MSD data were statistically averaged for independent simulations of 5 different configurations. Fig. 3(a) shows that the MSD of cations is close to zero and does not vary with time even at 1800 K. The cations exhibit only vibrational features on their lattice site. It would be worth noting that the oscillation amplitude of the doped cation Gd^{3+} (see the inset of Fig. 3(a)) is larger than that of the host cation Ce^{4+}. This would be due to the lower CN of doped Gd^{3+}. On the other hand, the MSD of oxygen anions linearly increases with time, reflecting notable diffusion of oxygen anions in the present MD simulation time. From the linear relationship, the diffusivity of the anion can be calculated using the Einstein relationship,[54] $\langle \Delta R^2 \rangle = 6\ D \times t$, where D is the diffusivity of ions. From the slope of MSD *vs.* time for various temperatures T (see Fig. 3(b)), diffusivity can be obtained as a function of temperature in the range from 1000 to 2000 K. The activation energy E_a of ion diffusion is then determined by using the Arrhenius equation of diffusivity[55] as shown in Fig. 3(c),

$$D = D_0 \exp\left(-\frac{E_a}{k_B T}\right) \quad (3)$$

Here k_B is the Boltzmann constant and D_0 is the pre-exponential term of diffusion. Table 2 summarizes the activation energies for oxygen diffusion in the doped ceria electrolytes. The

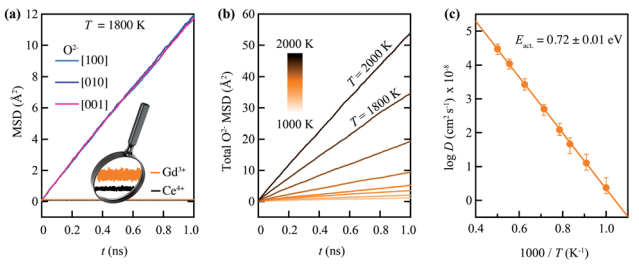

Fig. 3 (a) Mean square displacements $\langle R^2 \rangle$ for cations and oxygen ions (resolved in the orthogonal [001], [010], and [001] directions) for 10GDC (in sky blue, blue, and pink lines) at $T = 1800$ K for 1 ns. (b) The $\langle R^2 \rangle$ at various temperatures (T) for 10GDC. Temperature was monochromatically scaled in orange. Note that the slope of the graph reflects the ion diffusion coefficient D. (c) The Arrhenius plots of the diffusion coefficient (log D) as a function of $1000/T$ for the 10GDC system, and five randomized structures have been used for better statistics.

Table 2 Calculated activation energy barriers of oxygen ion migration for doped and co-doped ceria systems

Specimen	$E_a \pm \Delta E_a$
10GDC	0.72 ± 0.001
3Y7GDC	0.76 ± 0.002
3La7GDC	0.70 ± 0.001

activation energy for 10GDC was 0.72 ± 0.01 eV. The order of magnitude of this value agrees with the previous experimental results shown in Table 1 of ref. 56. We compared the simulated diffusion behavior of Gd, La, or Y doped ceria as shown in Fig. S3.† This simulation is consistent with previous experimental studies.[21] It can thus be said that the characterization of the diffusion by the MSD analysis is acceptable in the present work. Y^{3+} and La^{3+} co-doping exhibited a contrasting behavior. La^{3+} co-doping into 10GDC slightly reduced the activation energy for oxygen diffusion (0.70 ± 0.01 eV), while Y^{3+} co-doping increases the activation energy to 0.76 ± 0.02 eV.

The contrasting effect of co-doping on the diffusion behavior is in agreement with the site preference of the oxygen vacancy with the co-doped elements. As can be seen in the CN analysis of Fig. 2, oxygen vacancies interacted more preferentially with Y^{3+} than Gd^{3+}, while no preference of vacancies to the co-doped La^{3+} was observed. The reduced preference of oxygen vacancies to the La^{3+} dopant would increase the mobility of the oxygen vacancies. In contrast, Y^{3+} co-doping deteriorates the oxygen diffusion by trapping the oxygen vacancies. This observation would strongly support the fact that the mobility of the oxygen vacancy is significantly deteriorated by the preferential trapping into dopants.

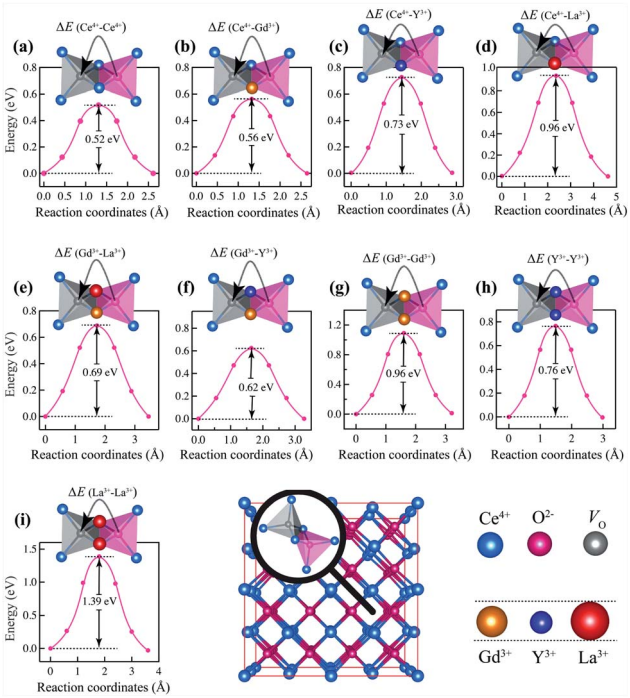

Fig. 4 Oxygen migration barrier between two adjacent tetrahedral oxygen sites in fluorite structured ceria with the migration edge of (a) Ce^{4+}–Ce^{4+}, (b) Ce^{4+}–Gd^{3+}, (c) Ce^{4+}–Y^{3+}, (d) Ce^{4+}–La^{3+}, (e) Gd^{3+}–La^{3+}, (f) Gd^{3+}–Y^{3+}, (g) Gd^{3+}–Gd^{3+}, (h) Y^{3+}–Y^{3+}, and (i) La^{3+}–La^{3+}, calculated from the first-principles NEB method. The structure given in (c), (d), (e), and (f) consists of one Gd and one co-doped (Y or La) ion with one oxygen vacancy, except for in (a) and (b) where the structure is respectively composed of pure ceria and two Gd-doped ions with one oxygen vacancy in a 2 × 2 × 2 supercell. The oxygen ion migration between two tetrahedrons with the given edges is shown systematically in the inset of each graph.

However, the dopant can also affect the migration barrier of oxygen ions, as previously referred to as "blocking energy".[21] In order to study the effect of doping on the blocking energy, we investigated the energy barrier of the oxygen vacancy migration in the symmetric configuration as shown in Fig. 4. We performed the first-principles NEB calculations for the oxygen vacancy to migrate across the edge of all possible combinations of doped cations: Ce^{4+}–Ce^{4+}, Ce^{4+}–Gd^{3+}, Ce^{4+}–Y^{3+}, Ce^{4+}–La^{3+}, Gd^{3+}–La^{3+}, Gd^{3+}–Y^{3+}, Gd^{3+}–Gd^{3+}, Y^{3+}–Y^{3+}, and La^{3+}–La^{3+}. In this symmetric configuration, the potential energy of oxygen vacancies is invariant with the migration.

Therefore, the energy barrier of the migration will represent the blocking energy only. Fig. 4 represents the computed energy barriers for various combinations of the doped cations. When we calculated the energy barrier with only one dopant at the tetrahedron edge (as in Fig. 4(b)–(d)), an additional Gd^{3+} dopant was placed in the supercell to consider the co-doped environment.

The results in Fig. 4(a), (b), and (g) show that the blocking energy was slightly increased by the Gd^{3+} doping. If La^{3+} was co-doped in GDC, there would exist five kinds of atomic configurations in the edge, Fig. 4(a), (b), (d), (e), (g), and (i). All the energy barriers of the co-doped cases were higher than in the Gd^{3+} doped case. Therefore, the effective blocking energy of the oxygen migration would considerably increase with the La^{3+} doping. The blocking energy also increased when Y^{3+} was co-doped into the GDC as can be seen in Fig. 4(a)–(c) and (f)–(h). The present NEB calculations showed that both La^{3+} and Y^{3+} co-doping increased blocking energy for oxygen diffusion across the tetrahedron edge. It must be noted that these results are not consistent with the diffusion behavior in co-doped GDC: oxygen diffusion was enhanced by co-doping of La^{3+}, whereas Y^{3+} co-doping degrades the oxygen diffusion (see Table 2). These findings support that the trapping of oxygen vacancies is more significant to understand the oxygen diffusion behavior in doped ceria electrolytes.

It was also revealed that the external strain affects the vacancy trapping behavior and thus the oxygen diffusion. We applied a series of lateral strain (biaxial strain) in the range of −2.5% to 2.5% along the *a* and *b* lattice directions to 10GDC, 3Y7GDC, and 3La7GDC. These simulation conditions are to model the GDC electrolyte films grown (partly epitaxially) on a substrate of different lattice constants. The stress–strain curve of the considered systems at various temperatures shows an

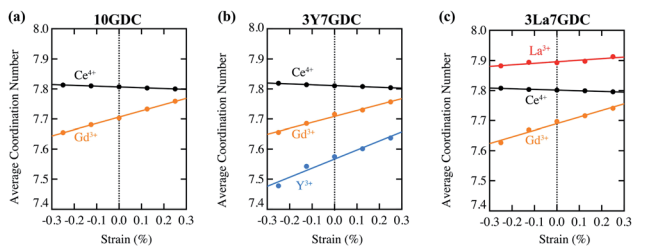

Fig. 5 The coordination number (CN) of cations to anions as a function of biaxial strain in (a) 10GDC, (b) 3Y7GDC, and (c) 3La7GDC systems at $T = 1273$ K.

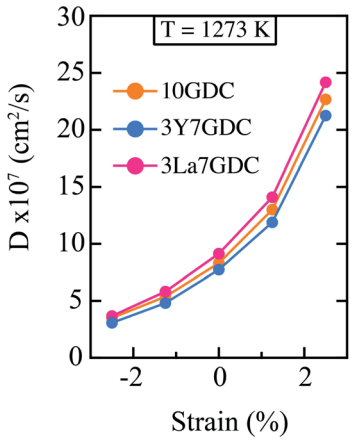

Fig. 6 The diffusion coefficient (D) as a function of equi-biaxial strain in the range of −2.5 to 2.5% for 10GDC, 3Y7GDC, and 3La7GDC systems at $T = 1273$ K.

elastic behavior up to 4.5% tensile strain (see Fig. S4†). Therefore, we can expect that the atomic structure of the film is maintained in this strain range. Fig. 5 shows the dependence of the coordination number (CN) on the applied strain. In 10GDC, the CN of doped Gd^{3+} significantly increased with the applied tensile strain, while that of Ce^{4+} slightly decreased (see Fig. 5(a)). This result reveals that the oxygen vacancy trapping into the doped cation (Gd^{3+}) is reduced by applying tensile strain. On the other hand, compressive strain enhanced the vacancy trapping tendency into the doped cation. An increase in the CN of dopants commonly occurs in Y^{3+} or La^{3+} co-doped specimens. In both cases, the CN of Ce^{4+} slightly decreases. The increased CN or reduced tendency of vacancy trapping has an effect to increase the diffusion. Fig. 6 shows the substantial increase of the oxygen diffusion coefficient at 1273 K as the tensile strain increases. However, one should note that the change in diffusivity appears almost the same in the three different co-doped systems, even if the sensitivity of the CN to the applied strain, as can be evaluated from the slope of Fig. 5, is larger for the smaller dopant. This would be due to the duplicating effect of external strain that changes not only the trapping energy (as shown in Fig. 5)[23] but also the blocking energy by changing the tetrahedron volume.[24]

4 Conclusions

We theoretically investigated oxygen diffusion in Gd^{3+} doped ceria (GDC) co-doped with Y^{3+} or La^{3+}. Characterizing the coordination number of cations and the diffusion simulation on a large scale disclosed the major factor to control the oxygen diffusion in ceria electrolytes. By combining with NEB calculation results, we could reveal that the change in oxygen diffusion is governed by the vacancy trapping behavior into the dopants. The co-doping of Y^{3+} that is smaller than Gd^{3+} enhanced the oxygen vacancy trapping into Y^{3+}, resulting in suppressed oxygen diffusion. When larger La^{3+} ions than Gd^{3+} were co-doped, oxygen diffusion was increased as the tendency of vacancy trapping into La^{3+} significantly decreased. In contrast, the blocking energy against oxygen migration between tetrahedron centers is estimated to increase in both Y^{3+} and La^{3+} co-doped cases. It was further shown that the external tensile strain reduced the difference in the vacancy trapping between the cations, which can improve the oxygen mobility and thus ion conductivity in the ceria-based electrolyte. However, the change in oxygen diffusion by external strain is not sensitive to the co-doped element since the external strain also changed the tetrahedron volume and thus the blocking energy against the oxygen migration. It would be more desirable that the dominating vacancy trapping effect is confirmed in a larger number of co-doping configurations. Coordination number analysis would be an effective approach to investigate the vacancy trapping behavior in a wide range of electrolyte systems. In addition, experimental verification of the co-doping effect with carefully prepared materials is also required.

Conflicts of interest

There are no conflicts to declare.

Acknowledgements

This work was supported by the Brain Pool Program through the National Research Foundation of Korea (NRF) funded by the Ministry of Science and ICT (2020H1D3A1A02081517) and the Nano Materials Research Program through the Ministry of Science and IT Technology under project No. NRF-2016M3A7B4025402. The computing environment was prepared by using Materials Square.

References

1 J. A. Kilner, *Solid State Ionics*, 2000, **129**, 13–23.
2 S. J. Skinner and J. A. Kilner, *Mater. Today*, 2003, **6**, 30–37.
3 M. Melchionna and P. Fornasiero, *Mater. Today*, 2014, **17**, 349–357.
4 B. C. Steele and A. Heinzel, *Nature*, 2001, **414**, 345–352.
5 D. Kashyap, P. Patro, R. Lenka, T. Mahata and P. Sinha, *Ceram. Int.*, 2014, **40**, 11869–11875.
6 S. Omar, E. D. Wachsman and J. C. Nino, *Solid State Ionics*, 2008, **178**, 1890–1897.
7 Y. P. Ivanov, M. Kubicek, M. Siebenhofer, A. Viernstein, H. Hutter, J. Fleig, A. Chuvilin and Z. Zhang, *Communications Materials*, 2020, **1**, 1–8.
8 G. F. Harrington, L. Sun, B. Yildiz, K. Sasaki, N. H. Perry and H. L. Tuller, *Acta Mater.*, 2019, **166**, 447–458.
9 D.-J. Kim, *J. Am. Ceram. Soc.*, 1989, **72**, 1415–1421.
10 H. Yamamura, E. Katoh, M. Ichikawa, K. Kakinuma, T. Mori and H. Haneda, *Electrochemistry*, 2000, **68**, 455–459.
11 F.-Y. Wang, S. Chen and S. Cheng, *Electrochem. Commun.*, 2004, **6**, 743–746.
12 Y. Zheng, H. Gu, H. Chen, L. Gao, X. Zhu and L. Guo, *Mater. Res. Bull.*, 2009, **44**, 775–779.
13 D. Park, J. Griffith, A. Nowick, *et al.*, *Solid State Ionics*, 1981, **2**, 95–105.

14 M. Mogensen, N. M. Sammes and G. A. Tompsett, *Solid State Ionics*, 2000, **129**, 63–94.
15 J. Faber, C. Geoffroy, A. Roux, A. Sylvestre and P. Abelard, *Appl. Phys. A: Solids Surf.*, 1989, **49**, 225–232.
16 V. Butler, C. Catlow, B. Fender and J. Harding, *Solid State Ionics*, 1983, **8**, 109–113.
17 L. Minervini, M. O. Zacate and R. W. Grimes, *Solid State Ionics*, 1999, **116**, 339–349.
18 H. Yahiro, K. Eguchi and H. Arai, *Solid State Ionics*, 1989, **36**, 71–75.
19 X. Wei, W. Pan, L. Cheng and B. Li, *Solid State Ionics*, 2009, **180**, 13–17.
20 H. Deguchi, H. Yoshida, T. Inagaki and M. Horiuchi, *Solid State Ionics*, 2005, **176**, 1817–1825.
21 J. Koettgen, S. Grieshammer, P. Hein, B. O. Grope, M. Nakayama and M. Martin, *Phys. Chem. Chem. Phys.*, 2018, **20**, 14291–14321.
22 M. Rushton and A. Chroneos, *Sci. Rep.*, 2014, **4**, 1–6.
23 M. Rushton, A. Chroneos, S. Skinner, J. Kilner and R. Grimes, *Solid State Ionics*, 2013, **230**, 37–42.
24 J. Ahn, S. Choi, K. J. Yoon, J.-W. Son, B.-K. Kim, J.-H. Lee, H. W. Jang and H. Kim, *ACS Appl. Mater. Interfaces*, 2017, **9**, 42415–42419.
25 R. A. De Souza, A. Ramadan and S. Hörner, *Energy Environ. Sci.*, 2012, **5**, 5445–5453.
26 M. Burbano, S. Nadin, D. Marrocchelli, M. Salanne and G. W. Watson, *Phys. Chem. Chem. Phys.*, 2014, **16**, 8320–8331.
27 Z. Fu, Q. Sun, D. Ma, N. Zhang, Y. An and Z. Yang, *Appl. Phys. Lett.*, 2017, **111**, 023903.
28 J. Kilner, *Faraday Discuss.*, 2007, **134**, 9–15.
29 J. Kilner and R. Brook, *Solid State Ionics*, 1982, **6**, 237–252.
30 G. Kresse and J. Hafner, *Phys. Rev. B: Condens. Matter Mater. Phys.*, 1993, **47**, 558.
31 G. Kresse and D. Joubert, *Phys. Rev. B: Condens. Matter Mater. Phys.*, 1999, **59**, 1758.
32 P. E. Blöchl, *Phys. Rev. B: Condens. Matter Mater. Phys.*, 1994, **50**, 17953.
33 J. P. Perdew, K. Burke and M. Ernzerhof, *Phys. Rev. Lett.*, 1996, **77**, 3865.
34 S. Dudarev, G. Botton, S. Savrasov, C. Humphreys and A. Sutton, *Phys. Rev. B: Condens. Matter Mater. Phys.*, 1998, **57**, 1505.
35 H. J. Monkhorst and J. D. Pack, *Phys. Rev. B: Solid State*, 1976, **13**, 5188.
36 G. Henkelman, B. P. Uberuaga and H. Jónsson, *J. Chem. Phys.*, 2000, **113**, 9901–9904.
37 S. Vyas, R. W. Grimes, D. H. Gay and A. L. Rohl, *J. Chem. Soc., Faraday Trans.*, 1998, **94**, 427–434.
38 R. W. Grimes, G. Busker, M. A. McCoy, A. Chroneos, J. A. Kilner and S.-P. Chen, *Ber. Bunsen. Phys. Chem.*, 1997, **101**, 1204–1210.
39 S. Plimpton, *J. Comput. Phys.*, 1995, **117**, 1–19.
40 J. D. Gale and A. L. Rohl, *Mol. Simul.*, 2003, **29**, 291–341.
41 S. Grieshammer, I. V. Belova and G. E. Murch, *Acta Mater.*, 2021, **210**, 116802.
42 M. E. Kilic and A. Soon, *J. Phys. Chem. C*, 2018, **122**, 22374–22388.
43 P. P. Ewald, *Ann. Phys.*, 1921, **369**, 253–287.
44 N. Skorodumova, R. Ahuja, S. Simak, I. Abrikosov, B. Johansson and B. Lundqvist, *Phys. Rev. B: Condens. Matter Mater. Phys.*, 2001, **64**, 115108.
45 S. Nosé, *Mol. Phys.*, 1984, **52**, 255–268.
46 S. Nosé, *J. Chem. Phys.*, 1984, **81**, 511–519.
47 W. G. Hoover, *Phys. Rev. A: At., Mol., Opt. Phys.*, 1985, **31**, 1695.
48 T. X. Sayle and D. C. Sayle, *ACS Nano*, 2010, **4**, 879–886.
49 L. Sun, D. Marrocchelli and B. Yildiz, *Nat. Commun.*, 2015, **6**, 1–10.
50 D.-H. Jung, J.-H. Lee, M. E. Kilic and A. Soon, *Phys. Chem. Chem. Phys.*, 2018, **20**, 10048–10059.
51 R. Grau-Crespo, S. Hamad, C. R. A. Catlow and N. De Leeuw, *J. Phys.: Condens. Matter*, 2007, **19**, 256201.
52 R. D. Shannon, *Acta Crystallogr., Sect. A: Cryst. Phys., Diffr., Theor. Gen. Crystallogr.*, 1976, **32**, 751–767.
53 I. Heinmaa, T. Joon, H. Kooskora, J. Pahapill and J. Subbi, *Solid State Ionics*, 2010, **181**, 1309–1315.
54 A. Einstein, *et al.*, *Ann. Phys.*, 1905, **17**, 208.
55 S. Arrhenius, *Z. Phys. Chem.*, 1889, **4**, 226–248.
56 B. C. Steele, *Solid State Ionics*, 2000, **129**, 95–110.